

# Constraining CO coverage on copper promotes high efficiency ethylene electroproduction

Jun Li, Ziyun Wang, Christopher McCallum, Yi Xu, Fengwang Li, Yuhang Wang, Christine Gabardo, Cao-Thang Dinh, Tao-Tao Zhuang, Liang Wang, Jane Y. Howe, Yang Ren, Edward H. Sargent & David Sinton

**Version** Post-print/Accepted Manuscript

**Citation (published version)** Li, J., Wang, Z., McCallum, C. et al. Constraining CO coverage on copper promotes high-efficiency ethylene electroproduction. *Nat Catal* 2, 1124–1131 (2019) doi:[10.1038/s41929-019-0380-x](https://doi.org/10.1038/s41929-019-0380-x)

## How to cite TSpace items

Always cite the published version, so the author(s) will receive recognition through services that track citation counts, e.g. Scopus. If you need to cite the page number of the **author manuscript from TSpace** because you cannot access the published version, then cite the TSpace version **in addition to** the published version using the permanent URI (handle) found on the record page.

This article was made openly accessible by U of T Faculty.  
Please [tell us](#) how this access benefits you. Your story matters.

1    Constraining CO coverage on copper promotes high-  
2    efficiency ethylene electroproduction

3    *Jun Li<sup>1,2†</sup>, Ziyun Wang<sup>2†</sup>, Christopher McCallum<sup>1†</sup>, Yi Xu<sup>1</sup>, Fengwang Li<sup>2</sup>, Yuhang Wang<sup>2</sup>,*  
4    *Christine Gabardo<sup>1</sup>, Cao-Thang Dinh<sup>2</sup>, Tao-Tao Zhuang<sup>2</sup>, Liang Wang<sup>3</sup>, Jane Y. Howe<sup>4</sup>, Yang*  
5    *Ren<sup>3</sup>, Edward H. Sargent<sup>2\*</sup> & David Sinton<sup>1\*</sup>*

6    <sup>1</sup>*Department of Mechanical and Industrial Engineering, University of Toronto, 5 King's College*  
7    *Road, Toronto, Ontario, M5S 3G8, Canada.*

8    <sup>2</sup>*Department of Electrical and Computer Engineering, University of Toronto, 10 King's College*  
9    *Road, Toronto, Ontario, M5S 3G4, Canada.*

10   <sup>3</sup>*Advanced Photon Source, Argonne National Laboratory, Lemont, Illinois, 60439, United States*

11   <sup>4</sup>*Hitachi High Technologies America, Inc., 22610 Gateway Center Drive, Suite 100, Clarksburg,*  
12   *Maryland 20871, USA*

13   <sup>†</sup>*These authors contributed equally: Jun Li, Ziyun Wang and Christopher McCallum.*

14   \*Corresponding email: [ted.sargent@utoronto.ca](mailto:ted.sargent@utoronto.ca); [sinton@mie.utoronto.ca](mailto:sinton@mie.utoronto.ca)

15

16 The availability of inexpensive industrial CO gas streams motivates efficient  
17 electrocatalytic upgrading to higher-value feedstocks such as ethylene. However, the  
18 electrosynthesis of ethylene via the CO reduction reaction (CORR) has suffered from low  
19 selectivity and energy efficiency. Here we find that the recent strategy, so effective in  
20 CO<sub>2</sub>RR, of increasing performance through the use of highly alkali electrolyte, fails in  
21 CORR and drives the reaction to acetate. We then observe that ethylene selectivity  
22 increases when we constrain (decrease) CO availability. Using density functional theory, we  
23 show how CO coverage on Cu influences the reaction pathways of ethylene versus  
24 oxygenate: lower CO coverage stabilizes the ethylene-relevant intermediates while higher  
25 CO coverage favours oxygenate formation. We then control local CO availability  
26 experimentally by tuning the CO concentration and reaction rate; we achieve ethylene  
27 Faradaic efficiencies of 72% and partial current density > 800 mA cm<sup>-2</sup>. The overall system  
28 provides a half-cell energy efficiency of 44% for ethylene production.

29

30 The electrochemical upgrading of CO<sub>2</sub> into carbon-based chemicals and fuels provides a  
31 means to close the anthropogenic carbon cycle and store excess renewable electricity<sup>1-3</sup>. Much  
32 effort has been dedicated to the production of valuable two-carbon (C<sub>2</sub>) products via direct CO<sub>2</sub>  
33 electrolysis<sup>4-7</sup>. Ethylene is an electrolysis product of particular interest in view of high demand  
34 for it, as a chemical feedstock.

35 Starting from CO, instead of CO<sub>2</sub>, as feedstock, avoids carbonate formation in alkaline CO<sub>2</sub>  
36 electrolyzers, and thus overcomes issues in feedstock utilization and stability<sup>8,9</sup>. Additionally,  
37 CO gas feedstock streams are available industrially at a range of purities. Abundant and  
38 inexpensive manufactured gases such as syngas, coal gas and producer gas, and also effluent  
39 streams from steel manufacturing, have CO concentrations in the range of 10% to 60%<sup>10-14</sup>. Gas  
40 purification from these streams is costly, as indicated by the sale price of high purity CO which  
41 is over ten times that of commercial CO streams having low purities (e.g. syngas)<sup>15</sup>. These costs  
42 will be avoided once available dilute CO gas streams – whether they be manufactured or effluent  
43 – are upgraded to ethylene with a high efficiency.

44 Recent advances in the CO reduction reaction (CORR) for ethylene production have focused  
45 on increasing the reaction rate and selectivity<sup>8,9,16-19</sup>. CO-to-ethylene at moderate current  
46 densities (~ 100 mA cm<sup>-2</sup>) has been demonstrated on nanostructured copper catalysts employing  
47 gas diffusion electrodes that overcome mass transfer limitations<sup>9,16-18</sup>. Increasing the alkalinity of  
48 the electrolyte has increased activity and selectivity for ethylene in both CO<sub>2</sub>RR<sup>4</sup> and CORR<sup>9</sup>.  
49 However, even with concentrated KOH electrolytes and pure CO reactant gas, the highest  
50 reported CO-to-ethylene Faradaic efficiency (FE) remains ~40% with a cathodic energy  
51 efficiency of ~20%<sup>9</sup>.

52 Here we present high-efficiency ethylene electroproduction from CO on Cu at current densities  
53 above 100 mA/cm<sup>2</sup>. The system performs well across a wide range of CO input concentrations.  
54 We find that increased ethylene selectivity is obtained when we decrease the CO availability up  
55 to the CO mass transport limit by operating at high current densities. This finding motivates us to  
56 investigate the link between local CO availability and ethylene selectivity. Using density  
57 functional theory (DFT) calculations, we first assess – as a function of CO coverage – the  
58 activation energies and enthalpy changes of the key elementary steps branching the ethylene  
59 versus the oxygenate pathways. We find that lowering CO coverage on copper benefits the  
60 ethylene pathway both thermodynamically and kinetically. In experiments, we constrain the local  
61 CO concentration at the catalyst:electrolyte interface by tuning the combination of CO supply  
62 concentration and reaction rate (e.g. applying high reaction rates for high input CO  
63 concentrations). Implementing this strategy, we achieve an ethylene partial current density >  
64 800 mA cm<sup>-2</sup> and an ethylene Faradaic efficiency over 70% across a wide range of CO  
65 concentrations (5 – 100%). Combining high selectivity with low overpotential we achieve a  
66 44% half-cell energy efficiency for ethylene production.

## 67 **Results**

### 68 **Effect of KOH concentration**

69 Hydroxide ions have – in the context of CO<sub>2</sub> reduction – been shown to play a crucial role in  
70 promoting both selectivity and activity in ethylene production. They do so when they bring the  
71 onset of ethylene production closer to that of CO<sup>4</sup>. A subsequent CORR flow cell study with  
72 increasing KOH concentration from 0.1 M to 1 M further demonstrated increased ethylene  
73 production via the suppression of hydrogen generation<sup>9</sup>.

74 To assess the effect of electrolyte alkalinity on ethylene production from CORR, we varied the  
75 KOH concentration from 1 M to 5 M and carried out CORR in highly alkaline conditions in a  
76 flow cell electrolyzer (**Supplementary Fig. 1**)<sup>4-6,20</sup>. Copper oxide pre-catalysts (see *Methods*)  
77 were deposited and then reduced to active Cu catalysts via CORR.

78 We found that increasing the alkalinity of the electrolyte above 1 M decreased ethylene  
79 electroproduction (**Fig. 1a**) and increased acetate formation (**Supplementary Fig. 2**). The  
80 increase of  $FE_{\text{acetate}}$  with elevated KOH concentration can be attributed to the reaction of  
81 concentrated hydroxide ions with CORR intermediates relevant to ethylene, ethanol and 1-  
82 propanol<sup>8,9,21</sup>. This interaction of hydroxide ions and intermediates is not significant in the case  
83 of alkaline  $\text{CO}_2$  electroreduction due to the pH-moderating influence of dissolved  $\text{CO}_2$ <sup>4</sup>, in which  
84 the concentration of hydroxide ions under  $\text{CO}_2$  reduction is more than one order of magnitude  
85 lower than under CORR at similar current and bulk electrolyte conditions<sup>9</sup>.

86 Under the electrolyte concentrations tested,  $FE_{\text{ethylene}}$  increased with applied potential/current  
87 (**Fig. 1a**), and peaked just prior to a sharp increase in hydrogen production (**Supplementary**  
88 **Fig. 3**). Specifically, increasing the potential from -0.2 to -0.6 V versus a reversible hydrogen  
89 electrode (vs. RHE) in 5 M KOH resulted in a linear increase of  $FE_{\text{ethylene}}$  (0.8 to 58%) and an  
90 exponential increase of ethylene partial current density (0.06 to 728  $\text{mA cm}^{-2}$ ) (**Fig. 1b**).  
91 Carrying out a reaction-diffusion model analysis, we found a dramatic decrease of local CO  
92 concentration at the catalyst layer due to increased reaction kinetics and thereby a buildup of  
93 hydroxide ions, i.e. an increase in local pH. A further increase of overpotential leads to severe  
94 depletion of local CO availability from rapid ethylene formation, a sharp increase of hydrogen  
95 binding and evolution (**Supplementary Fig. 4**), and thereby a reduction of  $FE_{\text{ethylene}}$ . The shift to

96 hydrogen signals the onset of CO mass transport limits, and represents the lower limit of CO  
97 availability for efficient ethylene production.

98 We then determined the cathodic energy efficiency for ethylene production from the measured  
99 overpotential and ethylene selectivity (**Supplementary Fig. 5** and **Supplementary Note 1**). The  
100 highest ethylene cathodic energy efficiency of 35% is achieved when we used 1 M KOH.  
101 Improving this energy efficiency further would require increased ethylene selectivity at lower  
102 overpotential. Results here (**Fig. 1**) indicate that increasing electrolyte alkalinity will not increase  
103 ethylene selectivity further; however, reaction-rate driven changes in local CO availability can  
104 influence ethylene selectivity. We therefore hypothesized that independently controlling local  
105 CO concentration at the catalyst surface could offer a route to advance ethylene production  
106 efficiency.

### 107 **Density functional theory calculations**

108 We sought to understand, with the aid of DFT, the connection between local CO concentration  
109 and the ethylene versus oxygenate formation pathways. Previous reports correlate  
110 ethylene/oxygenate production from CO reduction with the hydrogenation of oxygen-containing  
111 intermediates<sup>22-24</sup>, indicating that once all the oxygen-containing groups are removed by  
112 hydrogenation to form water, the intermediate state is likely to proceed towards ethylene.  
113 Specifically, \*CHCOH (denoted IM, **Fig. 2a**) has been identified as the key intermediate for  
114 hydrogenation into both ethylene and oxygenates<sup>23</sup>, in which the hydroxyl group can be  
115 deoxidized forming \*CCH (IM-C), leading to ethylene. The intermediate can instead be  
116 hydrogenated into \*CHCHOH (IM-O), favouring the production of oxygenates. We wondered  
117 whether controlling the IM reduction step to encourage the C-pathway (IM-C) instead of the O-  
118 pathway (IM-O) could promote ethylene production.

119 Using DFT calculations, we predicted the geometries of IM, IM-C, and IM-O on Cu(100) (**Fig.**  
120 **2a**). We note that the main difference between the IM-O and IM-C intermediate state is the  
121 degree of unsaturation (**Supplementary Note 2**), namely 2.5 for IM-C and 1.5 for IM-O. Thus  
122 IM-C requires more surface bonding ability in order to be stabilized. As the adsorption of  
123 intermediates is affected by the surface coverage of CO due to adsorbate-adsorbate interactions<sup>25</sup>,  
124 tuning the surface bonding ability of IM-C by controlling the coverage of adsorbed \*CO could  
125 influence the relative stability of ethylene-forming IM-C vs. IM-O.

126 We first calculated the reaction energies of the C-pathway and O-pathway (**Fig. 2b**). The  
127 reaction energies for these pathways are similar at zero CO coverage, and the O-pathway  
128 becomes more favorable at higher CO coverages. Noting the key role of kinetics in these  
129 reactions<sup>22</sup>, we used an explicit water model to calculate the energies of the three intermediate  
130 states (IM, IM-C, IM-O) and associated transition states (TS-C and TS-O) with coverage of \*CO  
131 ranging from 0 to 3/9 (**Supplementary Fig. 6-15**)<sup>26</sup>. A coverage of 3/9 was selected based on a  
132 kinetic modelling prediction of ~0.3 ML CO coverage on Cu surfaces<sup>27</sup>. We found the barriers to  
133 both the C-pathway and the O-pathway increase with increasing CO coverage (**Fig. 2c**). At low  
134 CO coverage the C-pathway is kinetically favoured over the O-pathway, and the O-pathway  
135 becomes more favourable at 3/9 ML. These models do not indicate the species expected: acetate,  
136 ethanol and 1-propanol. However, both the reaction energy and enthalpy calculations indicate  
137 that an oxygenate-forming O-pathway is favoured at higher CO coverages.

138 We also calculated the effects of CO coverage on the CO dimerization barriers and enthalpy  
139 changes (**Supplementary Fig. 16-22**). Both show decreased values as CO coverage increases,  
140 indicating that high CO coverage favors CO dimerization. The barrier to CO dimerization at 2/9  
141 ML, with two CO reactants and no other adsorbed CO, is calculated to be 0.66 eV, which is



142 lower than the threshold (0.75 eV) for fast kinetics<sup>28</sup>, and suggests that dimerization is not  
143 limiting under these conditions. We further assessed the barriers of the C-pathway and O-  
144 pathway with applied potentials (**Supplementary Fig. 23**)<sup>27,29</sup>. These barriers are lower than  
145 those associated with CO dimerization at similar CO coverages, suggesting that CO dimerization  
146 is the rate-determining step, consistent with previous findings<sup>28,30</sup>.

147 These DFT simulations predict that limiting the surface coverage of CO would favour ethylene  
148 production. In practice, CO coverage can be limited by increasing the reaction rate, but not  
149 without higher overpotentials and reduced efficiency. An independent means of controlling CO  
150 coverage is via the local CO concentration ( $[CO]$ ) or CO pressure ( $P_{CO}$ ), where  $[CO]$  correlates  
151 with  $P_{CO}$  via Henry's law. At equilibrium, the surface coverage of CO ( $\theta_{CO}$ ) is directly  
152 proportional to the local CO partial pressure, as given by equation<sup>31,32</sup>:

$$153 \quad \theta_{CO} = \theta_* P_{CO} e^{-\frac{E_{CO}}{RT}} \quad (1)$$

154 where  $\theta_*$  is the coverage of free surface sites.  $E_{CO}$  is the CO adsorption energy on the surface.  
155 R and T are the ideal gas constant and temperature, respectively. Therefore, to achieve low  
156 coverage of CO favoring ethylene production, decreasing the partial pressure of CO at catalysts  
157 layer is a promising approach.

### 158 **Materials characterization**

159 To explore experimentally the implications of the DFT results, we pursued CORR with a wide  
160 range of CO supply gas concentrations via dilution with N<sub>2</sub>, beginning with in situ catalyst  
161 derivation (**Fig. 3a**). Cu catalysts derived from oxide precatalysts (**Supplementary Fig. 24**) at  
162 CO concentration of 100% (**Fig. 3b**) and 2.5% (**Fig. 3c**) show similar morphology of aggregated  
163 nanoparticle structures. Operando X-ray absorption spectra at the Cu K-edge exhibit pure

164 metallic Cu features from catalysts derived at all tested CO concentrations (**Fig. 3d** and  
165 **Supplementary Fig. 25**). High-resolution operando X-ray diffraction analysis<sup>33</sup> further confirms  
166 that a stable metallic Cu structure remains the active catalyst during CORR operation under these  
167 conditions (**Fig. 3e** and **Supplementary Fig. 26**).

### 168 **Influence of CO gas concentration**

169 We evaluated CORR performance as a function of input CO gas concentration in 1 M KOH  
170 with a range of applied potentials. When we varied the incoming CO concentration from 2.5 to  
171 100% (within an inert N<sub>2</sub> carrier gas), we observed an overall increase of both total current  
172 density (**Supplementary Fig. 27**) and CORR partial current density (**Fig. 4a** and **4b**). The  
173 enhancement of current density follows an exponential increase within the potential window of –  
174 0.32 V to –0.52 V vs. RHE at CO concentrations of 2.5%, 5% and 10%. The exponential trend  
175 extends further to potentials of -0.66V and -0.72 V vs. RHE at the highest CO concentrations of  
176 50% and 100%, respectively. These trends indicate abundant mass transport (no mass transport  
177 limitation) over these potential ranges<sup>9</sup>. At higher overpotential, the current density trend is  
178 curbed due to CO mass transport limitation (**Fig. 4a, 4b** and **Supplementary Fig. 27**)<sup>8</sup>, with a  
179 characteristic increase in hydrogen production (**Supplementary Fig. 28**).

180 Ethylene FE increases with applied potential to a peak value corresponding to the onset of  
181 mass transport limitation observed in the current output (**Fig. 4c** and **4d**). The result is a similar  
182 ethylene partial current density when operating at different CO concentrations without CO mass  
183 transport limitation (**Supplementary Fig. 29**), in agreement with a previous report<sup>34</sup>. With 2.5%  
184 CO, a peak FE of 51% is reached, commensurate with a 32% FE of hydrogen at -0.53 vs. RHE  
185 (**Supplementary Fig. 28**). For cases of CORR performed at 5% and 10% CO conditions, we  
186 achieve 72% FE<sub>ethylene</sub> at -0.52 V vs. RHE with a significant decrease of hydrogen production

187 **(Supplementary Fig. 28)**. Further increasing the CO concentration to 50% and 100% results in  
188 peak ethylene production of ~70% at higher potentials of -0.66 V and -0.72 V vs. RHE, with  
189 ethylene partial current densities of 509 mA cm<sup>-2</sup> and 808 mA cm<sup>-2</sup>, respectively. By leveraging the  
190 dependence of overpotential and ethylene selectivity on input CO concentration, we achieved 44%  
191 cathodic energy efficiency for ethylene production, as did so using 5% CO **(Supplementary**  
192 **Note 1)**. These results surpass the best reported CORR FE<sub>ethylene</sub> (~40%) achieved at a potential  
193 of -0.72 V vs. RHE (equivalent to a ~24% increase in cathodic energy efficiency)<sup>9</sup> by a factor of  
194 1.6 in ethylene selectivity; and by a factor of 1.8 in cathodic energy efficiency. It represents the  
195 most efficient electrocatalytic CO-to-ethylene conversion reported to date **(Supplementary**  
196 **Table 1)**. To assess further ethylene formation among only carbon-based products, we  
197 normalized ethylene selectivity by excluding the H<sub>2</sub> contribution. The normalized FE<sub>ethylene</sub> first  
198 increases and then reaches a plateau at a value of ~75% **(Supplementary Fig. 30)**, which further  
199 supports the view that limiting CO availability on Cu stabilizes intermediates favourable for  
200 ethylene.

201 To gain further insight into this ethylene formation strategy, we performed CORR in 1 M  
202 KOH at various CO concentrations and a fixed potential of -0.44 V vs. RHE. With pure CO  
203 (100%), we observed a wide distribution of FEs for various products **(Fig. 4e)**, in agreement with  
204 a recent CORR report<sup>9</sup>. Ethylene was the dominant product with an FE of ~30%. When we  
205 decreased the CO concentration from 100 to 5%, FE<sub>ethylene</sub> increased to ~50% at the expense of  
206 FE<sub>1-propanol</sub>, and with little impact on FE<sub>acetate</sub>, FE<sub>ethanol</sub> and FE<sub>H2</sub>, confirming that an avenue to  
207 increase FE<sub>ethylene</sub> is to constrain CO. We noted a slight decrease of current densities at reduced  
208 CO concentrations, a feature we attributed to the lack of CO reactant and thus sluggish CORR  
209 kinetics at these conditions **(Supplementary Fig. 31)**.

210 With a further decrease of CO concentration from 5 to 2.5%, the lack of CO reactant manifests  
211 in significant hydrogen production. This ethylene selectivity decrease highlights the fact that low  
212 CO availability promotes ethylene production only up to the mass transport limit. When the CO  
213 availability is decreased beyond the mass transport limit, either by increasing the reaction  
214 rate/potential at a fixed CO concentration (**Fig. 4a-d**) or lowering the input CO concentration at a  
215 fixed reaction rate/potential (**Fig. 4e** and **Supplementary Fig. 32**), ethylene selectivity reduces,  
216 in agreement with previous studies<sup>19,35</sup>. The key to ethylene production from CO is thus to  
217 constrain operating conditions such that CO availability is neither too high (promoting  
218 oxygenates) nor too low (promoting hydrogen).

219 The normalized  $FE_{\text{ethylene}}$  (without hydrogen) shows a smooth trend of increased ethylene  
220 production with decreasing CO concentration, in all cases (**Fig. 4f**). In terms of carbon products,  
221 we produce almost exclusively  $C_2$  at low CO conditions (~70% of ethylene and ~25% of ethanol  
222 at a 2.5% CO condition), and we observe a product switching from ethylene to 1-propanol at  
223 higher CO concentrations. The development of operando/in-situ techniques capable of tracking  
224 key  $C_{2+}$  intermediates<sup>36</sup> while operating at conditions relevant to flow cells would further our  
225 understanding of the C- and O-pathway branching in these systems.

226 The ethylene production performance measured with Faradaic efficiency, current density and  
227 cathodic energy efficiency demonstrates a wide operating zone (**Fig. 4g**). By tuning conditions to  
228 constrain local CO availability, we achieve ethylene FEs (65 to 72%), and high cathodic energy  
229 efficiencies (35 to 44%), with current densities (120 to 1250  $\text{mA cm}^{-2}$ ) well above the 100  $\text{mA}$   
230  $\text{cm}^{-2}$  threshold. We further tested the system by reacting a simulated coke oven gas  
231 (**Supplementary Fig. 33**), a by-product of industrial coke production in steel manufacturing,  
232 with a gaseous composition of 10% CO, 30% methane and 60% hydrogen<sup>37,38</sup>. We achieved

233 stable CORR with this industrial mixture, producing  $FE_{\text{ethylene}}$  of ~71% in 1 M KOH at a constant  
234 current density of  $150 \text{ mA cm}^{-2}$ .

235 For the conditions studied, we calculated the local CO concentration using a reaction-diffusion  
236 model, and plot it with the potential and Faradaic efficiency values that together determine  
237 cathodic energy efficiency (**Fig. 4h**). The highest selectivities for ethylene correspond to low  
238 local CO concentrations, and are retained over a wide potential window from -0.5 to -0.8V. The  
239 most energy-efficient combination of high selectivity and low overpotential occurs uniquely for  
240 low CO input stream concentrations.

## 241 **Discussion**

242 The findings of prior reports assessing the effect of CO partial pressure on ethylene  
243 electroproduction are varied. Schreier and co-workers<sup>34</sup> reported an unaltered ethylene partial  
244 current density with varying CO concentration from 100% to 10%, while Li and co-workers<sup>19</sup>  
245 showed a decreasing ethylene partial current density at lower CO partial pressures. We found  
246 that these findings can be unified on the basis of CO availability. When we start from CO-rich  
247 conditions (i.e. not limited by CO mass transport), decreasing CO partial pressure increases  
248 ethylene selectivity, but a decrease of total current density (due to sluggish reaction kinetics at  
249 low CO concentrations) leads to little change in the ethylene partial current density  
250 (**Supplementary Fig. 29**), in agreement with the report by Schreier and co-workers<sup>34</sup>. In  
251 contrast, Li and co-workers<sup>19</sup> reduced CO partial pressure from the initial condition of peak  
252 ethylene production from 100% CO feed. Under these CO-deficient conditions we also found  
253 that any decrease in the local CO concentration decreases ethylene selectivity, current density  
254 and ethylene partial current density (**Supplementary Fig. 32**).

255 The CO scarcity effect may play a role in ethylene production from CO<sub>2</sub> reduction<sup>4,39,40</sup>.  
256 Specifically, a wide potential gap of 200-300 mV for CO and ethylene formation has been  
257 observed from CO<sub>2</sub> reduction on Cu catalysts<sup>4,41,42</sup>, and the concentration of as-formed \*CO  
258 intermediates on Cu is low. In CO<sub>2</sub>RR, concentrated hydroxide ions accelerate the rate-  
259 determining step of CO<sub>2</sub>RR (i.e. CO<sub>2</sub> to CO)<sup>4</sup>, bridge the potential gap between CO and ethylene,  
260 and also serve to limit local CO availability as the high pH electrolyte reduces the available CO<sub>2</sub>  
261 concentration. In contrast, direct CORR achieves higher local CO concentration on Cu and risks  
262 diverting ethylene formation to other products. A high concentration of CO promotes CO  
263 dimerization, and leads to a higher density of \*C<sub>2</sub> intermediates at the catalysts-electrolyte  
264 interface. Within a highly alkaline electrolyte these accumulated \*C<sub>2</sub> species react with the  
265 abundant hydroxide to form acetate<sup>9</sup>. At more moderate pH the \*C<sub>2</sub> can be further reduced to a  
266 C<sub>3</sub> product, i.e. 1-propanol, resulting from an intermolecular C-C coupling between \*C<sub>2</sub> and  
267 adsorbed \*CO species<sup>17,18</sup>. Constraining local CO availability at catalyst surfaces in CORR by  
268 tuning the incoming gas concentration and reaction rate, provides the route to efficient ethylene  
269 production.

270 CO-induced surface restructuring of Cu into nanoclusters has been shown to enhance the  
271 catalytic activity of Cu<sup>43-45</sup>. To assess the potential role of Cu nanoclusters in our system, we  
272 carried out CO partial pressure dependent tests using commercial polycrystalline Cu as  
273 electrocatalysts. In contrast to oxide-derived Cu, polycrystalline Cu does not produce  
274 nanoclusters during CORR<sup>38</sup>, nor does it exhibit product-specific sites for C<sub>2+</sub> formations<sup>21,45</sup>.  
275 The measured ethylene selectivity of polycrystalline Cu, as a function of CO partial pressure  
276 (**Supplementary Fig. 34**), was similar to that of oxide-derived Cu (**Fig. 4e**). We conclude that

277 ethylene selectivity is dominated by CO availability, and any surface restructuring in oxide-  
278 derived Cu plays a less role.

279 In summary, tuning local CO concentration at the catalyst surface enables efficient ethylene  
280 electrosynthesis. Constraining local CO availability on the Cu surface favours ethylene  
281 production, a trend seen both in simulations and experiments. We achieved  $\sim 70\%$  of  $FE_{\text{ethylene}}$   
282 over a wide range of CO concentrations, and ethylene partial current density of  $\sim 808 \text{ mA cm}^{-2}$ .  
283 With this strategy we combine low overpotential and high selectivity to achieve 44% half-cell  
284 ethylene energy efficiency. The performance here demonstrates efficient CO conversion to high-  
285 value  $C_2$  chemicals exceeding previous reports in terms of the critical metrics of output purity,  
286 energy efficiency and current density. Achieving these performance metrics with a dilute  
287 incoming stream presents additional opportunities to convert dilute effluent streams directly into  
288 concentrated valued products.

289

## 290 **Methods**

### 291 **DFT calculations**

292 In this work, all the DFT calculations were carried out with a periodic slab model using the  
293 Vienna *ab initio* simulation program (VASP)<sup>46-49</sup>. The generalized gradient approximation  
294 (GGA) was used with the Perdew-Burke-Ernzerhof (PBE)<sup>50</sup> exchange-correlation functional.  
295 The projector-augmented wave (PAW) method<sup>51,52</sup> was utilized to describe the electron-ion  
296 interactions, and the cut-off energy for the plane-wave basis set was 450 eV. In order to illustrate  
297 the long-range dispersion interactions between the adsorbates and catalysts, we employed the D3  
298 correction method by Grimme et al.<sup>53</sup> Brillouin zone integration was accomplished using a  
299  $3 \times 3 \times 1$  Monkhorst-Pack k-point mesh. Adsorption geometries were optimized using a force-  
300 based conjugate gradient algorithm, while transition states (TSs) were located with a constrained

301 minimisation technique<sup>54-56</sup>. At the intermediate and transition states, one charged layer of water  
302 molecules was added to the surface to take the combined field and solvation effects into  
303 account<sup>26</sup>. For the modelling of Cu(100), the crystal structure was optimized, and Cu(100) was  
304 modelled with a periodic four-layer p(3×3) model with the 2 lower layers fixed and 2 upper  
305 layers relaxed. The atomic coordinates of the optimised models, including the structures of initial  
306 states and transition states, are provided in **Supplementary Data 1**.

### 307 **Preparation of electrocatalysts and a gas diffusion electrode**

308 All reagents used in this work were from *Sigma Aldrich* without further purification. Simply put,  
309 copper oxide pre-catalysts were synthesized using a method reported earlier<sup>57</sup>. First 4.5 g triblock  
310 copolymer Pluronic P123 (MW 5800) was dispersed in 200 mL deionized water under a  
311 continuous stirring to form a clear solution. The 20 mL dark blue solution consisting of 0.4 g  
312 copper(II) fluoride (CuF<sub>2</sub>·2H<sub>2</sub>O), 3 mL ammonia (~30%) and deionized water was added and  
313 stirred to mix well. Last, 0.6 M L-ascorbic acid solution was made and added drop-by-drop into  
314 the above solution using a syringe until an orange suspension was formed, indicating the  
315 formation of copper oxide nanoparticles. The as-made product was rinsed with ethanol,  
316 centrifuged three times, and dried overnight under vacuum at room temperature (~20 °C). The  
317 preparation of a gas diffusion electrode (GDE) was made by air-brushing (N<sub>2</sub> as a carrier gas) a  
318 pre-catalyst ink consisting of 30 mg of as-made oxide-precatalysts, 3 mL isopropanol and 120 μL  
319 Nafion solution (~5 wt.%), onto a commercial Sigracet gas diffusion layer (GDL, Fuel Cell  
320 store) with a size of 4 × 6 cm<sup>2</sup>. The areal loading amount is ~1 mg cm<sup>-2</sup>. After vacuum drying, a  
321 2 × 2 cm<sup>2</sup> of GDE was cut and assembled into a flow cell electrolyser (**Supplementary Fig. 1**).  
322 Active Cu electrocatalysts were then derived under operando CORR condition.

### 323 **Characterization**



324 Surface morphology was analyzed using a Hitachi SU9000 SEM/STEM at 2 kV. Operando  
325 hard X-ray absorption spectroscopy measurements were conducted at beamline 9BM of the  
326 Advanced Photon Source (APS, Argonne National Laboratory, Lemont, Illinois). High-  
327 resolution operando XRD tests were performed at the beamline 11-ID ( $\lambda = 0.4593 \text{ \AA}$ ) of APS  
328 using a home-made flow cell (**Supplementary Fig. 26**). Operando measurements were  
329 performed at  $100 \text{ mA cm}^{-2}$  in 1 M KOH.

### 330 **Electrochemical reduction of carbon monoxide**

331 All CO reduction experiments were performed using a three-electrode flow cell electrolyser  
332 (see detailed sketches of flow reactor design in **Supplementary Fig. 1**)<sup>4,58</sup>. As-made GDE,  
333 Ag/AgCl (filled with 1 M KCl) and nickel foam (1.6 mm thickness, MTI Corporation) were used  
334 as cathode, reference electrode and anode, respectively. Alkaline solutions with various KOH  
335 concentrations were used as electrolytes at both cathode and anode sides. An anion exchange  
336 membrane (Fumasep FAA-PK-130) was sandwiched between catholyte and anolyte  
337 compartments to avoid product crossover. An Autolab PGSTAT204 (Metrohm Autolab) in  
338 combination with a BOOSTER10A module (Metrohm Autolab) was used as a power supply.  
339 During a CORR experiment, aqueous KOH solution was individually directed into and circulated  
340 through the cathode and anode compartments with the assistance of two variable-speed  
341 peristaltic tubing pumps (Control Company 3385). A 60 s.c.c.m. continuous flowing CO gas or  
342 CO/N<sub>2</sub> mixed gas was directed into the gas compartment and reacted at the catalyst-catholyte  
343 interface via gas diffusion through the GDL.

344 Applied cathode potentials after *iR* compensation were converted to the reversible hydrogen  
345 electrode (RHE) reference scale using  $E_{\text{RHE}} = E_{\text{Ag/AgCl}} + 0.235 \text{ V} + 0.059 \times \text{pH}$ . An *iR*  
346 compensation was performed using the equation:

347 
$$E_{iR} = E_{\text{applied}} - 0.85 * I_{\text{total}} * R \quad (2)$$

348 where  $E_{iR}$  is the  $iR$  corrected potential at the cathode,  $E_{\text{applied}}$  is the applied potential before  $iR$   
349 correction,  $I_{\text{total}}$  is the total current (a negative value at the cathode).  $R$  is the cell resistance with a  
350 value of 3.31  $\Omega$  obtained by performing an electrochemical impedance spectroscopy  
351 measurement using an Autolab PGSTAT302N electrochemical workstation coupled with a  
352 FRA32M module. A factor of 0.85 is applied in  $iR$  compensation during flow cell operation due  
353 to a low resistivity of 1 M KOH electrolyte which holds a relatively low voltage drop over the  
354 electrolyte.

355 Gas and liquid products were respectively analyzed using a gas chromatograph (GC,  
356 PerkinElmer Clarus 680) and a one-dimensional  $^1\text{H}$  Nuclear magnetic resonance spectroscopy  
357 ( $^1\text{H}$  NMR) coupled with a Agilent DD2 500 spectrometer<sup>4</sup>, in which a diluted Dimethyl  
358 sulfoxide (DMSO) in  $\text{D}_2\text{O}$  was used as an internal standard for the identification and  
359 quantification of liquid products.

360 Faradaic efficiency (FE) of ethylene was calculated using the equation<sup>9</sup>:

361 
$$\text{FE (\%)} = \frac{nFxV}{j_{\text{Total}}} \times 100 \quad (3)$$

362 where  $n$  is the number of electrons transferred,  $F$  is Faraday's constant,  $x$  is the mole fraction  
363 of ethylene,  $V$  is the total molar flow rate of gas reactant and  $j_{\text{Total}}$  is the total current applied  
364 during CORR.

365

### 366 **COMSOL modeling**

367 The CO and  $\text{OH}^-$  concentrations were modeled in COMSOL (COMSOL Multiphysics,  
368 Stockholm, Se) using a 1D reaction-diffusion model as outlined in **Supplementary Note 3**.

369 **Data availability.** The data that support the findings of this study are available from the  
370 corresponding author on reasonable request.

371

## 372 **References**

- 373
- 374 1 Seh, Z. W. *et al.* Combining theory and experiment in electrocatalysis: Insights into  
375 materials design. *Science* **355**, 146 (2017).
  - 376 2 Zhang, L., Zhao, Z. J. & Gong, J. L. Nanostructured materials for heterogeneous  
377 electrocatalytic CO<sub>2</sub> reduction and their related reaction mechanisms. *Angew. Chem., Int.*  
378 *Ed.* **56**, 11326-11353 (2017).
  - 379 3 Zheng, X. L. *et al.* Theory-guided Sn/Cu alloying for efficient CO<sub>2</sub> electroreduction at  
380 low overpotentials. *Nat. Catal.* **2**, 55-61 (2019).
  - 381 4 Dinh, C. T. *et al.* CO<sub>2</sub> electroreduction to ethylene via hydroxide-mediated copper  
382 catalysis at an abrupt interface. *Science* **360**, 783-787 (2018).
  - 383 5 De Luna, P. *et al.* Catalyst electro-redeposition controls morphology and oxidation state  
384 for selective carbon dioxide reduction. *Nat. Catal.* **1**, 103-110 (2018).
  - 385 6 Zhuang, T. T. *et al.* Steering post-C-C coupling selectivity enables high efficiency  
386 electroreduction of carbon dioxide to multi-carbon alcohols. *Nat. Catal.* **1**, 421-428  
387 (2018).
  - 388 7 Zhou, Y. S. *et al.* Dopant-induced electron localization drives CO<sub>2</sub> reduction to C<sub>2</sub>  
389 hydrocarbons. *Nat. Chem.* **10**, 974-980 (2018).
  - 390 8 Li, C. W., Ciston, J. & Kanan, M. W. Electroreduction of carbon monoxide to liquid fuel  
391 on oxide-derived nanocrystalline copper. *Nature* **508**, 504-507 (2014).
  - 392 9 Jouny, M., Luc, W. & Jiao, F. High-rate electroreduction of carbon monoxide to multi-  
393 carbon products. *Nat. Catal.* **1**, 748-755 (2018).
  - 394 10 Liu, M. *et al.* Enhanced electrocatalytic CO<sub>2</sub> reduction via field-induced reagent  
395 concentration. *Nature* **537**, 382-386 (2016).
  - 396 11 Haas, T., Krause, R., Weber, R., Demler, M. & Schmid, G. Technical photosynthesis  
397 involving CO<sub>2</sub> electrolysis and fermentation. *Nat. Catal.* **1**, 32-39 (2018).
  - 398 12 Schreier, M. *et al.* Solar conversion of CO<sub>2</sub> to CO using earth-abundant electrocatalysts  
399 prepared by atomic layer modification of CuO. *Nat. Energy* **2**, 17087 (2017).
  - 400 13 Li, J. *et al.* Efficient electrocatalytic CO<sub>2</sub> reduction on a three-phase interface. *Nat. Catal.*  
401 **1**, 592-600 (2018).
  - 402 14 Spurgeon, J. M. & Kumar, B. A comparative techno-economic analysis of pathways for  
403 commercial electrochemical CO<sub>2</sub> reduction to liquid products. *Energy Environ. Sci.* **11**,  
404 1536-1551 (2018).
  - 405 15 Jouny, M., Luc, W. & Jiao, F. General techno-economic analysis of CO<sub>2</sub> electrolysis  
406 systems. *Ind. Eng. Chem. Res.* **57**, 2165-2177 (2018).
  - 407 16 Han, L. H., Zhou, W. & Xiang, C. X. High-rate electrochemical reduction of carbon  
408 monoxide to ethylene using Cu-nanoparticle-based gas diffusion electrodes. *ACS Energy*  
409 *Lett.* **3**, 855-860 (2018).
  - 410 17 Zhuang, T. T. *et al.* Copper nanocavities confine intermediates for efficient  
411 electrosynthesis of C<sub>3</sub> alcohol fuels from carbon monoxide. *Nat. Catal.* **1**, 946-951  
412 (2018).

413 18 Pang, Y. J. *et al.* Efficient electrocatalytic conversion of carbon monoxide to propanol  
414 using fragmented copper. *Nat. Catal.* **2**, 251-258 (2019).

415 19 Li, J. *et al.* Effectively increased efficiency for electroreduction of carbon monoxide  
416 using supported polycrystalline copper powder electrocatalysts. *ACS Catal.* **9**, 4709-4718  
417 (2019).

418 20 Gabardo, C. M., Seifitokaldani, A., Edwards, J. P., Dinh, C. T., Burdyny, T., Kibria, M.  
419 G., O'Brien, C. P., Sargent, E. H. & Sinton, D. Combined high alkalinity and  
420 pressurization enable efficient CO<sub>2</sub> electroreduction to CO. *Energy Environ. Sci.* **11**,  
421 2531-2539 (2018).

422 21 Lum, Y. W. & Ager, J. W. Evidence for product-specific active sites on oxide-derived Cu  
423 catalysts for electrochemical CO<sub>2</sub> reduction. *Nat. Catal.* **2**, 86-93 (2019).

424 22 Xiao, H., Cheng, T. & Goddard, W. A. Atomistic mechanisms underlying selectivities in  
425 C<sub>1</sub> and C<sub>2</sub> products from electrochemical reduction of CO on Cu(111). *J. Am. Chem. Soc.*  
426 **139**, 130-136 (2017).

427 23 Lum, Y. W., Cheng, T., Goddard, W. A. & Ager, J. W. Electrochemical CO reduction  
428 builds solvent water into oxygenate products. *J. Am. Chem. Soc.* **140**, 9337-9340 (2018).

429 24 Cheng, T., Xiao, H. & Goddard, W. A. Full atomistic reaction mechanism with kinetics  
430 for CO reduction on Cu(100) from ab initio molecular dynamics free-energy calculations  
431 at 298 K. *Proc. Natl. Acad. Sci. U. S. A.* **114**, 1795-1800 (2017).

432 25 Lausche, A. C. *et al.* On the effect of coverage-dependent adsorbate-adsorbate  
433 interactions for CO methanation on transition metal surfaces. *J. Catal.* **307**, 275-282  
434 (2013).

435 26 Montoya, J. H., Shi, C., Chan, K. & Nørskov, J. K. Theoretical insights into a CO  
436 dimerization mechanism in CO<sub>2</sub> electroreduction. *J. Phys. Chem. Lett.* **6**, 2032-2037  
437 (2015).

438 27 Liu, X. Y. *et al.* Understanding trends in electrochemical carbon dioxide reduction rates.  
439 *Nat. Commun.* **8**, 15438 (2017).

440 28 Sandberg, R. B., Montoya, J. H., Chan, K. & Nørskov, J. K. CO-CO coupling on Cu  
441 facets: Coverage, strain and field effects. *Surf. Sci.* **654**, 56-62 (2016).

442 29 Nørskov, J. K. *et al.* Origin of the overpotential for oxygen reduction at a fuel-cell  
443 cathode. *J. Phys. Chem. B* **108**, 17886-17892 (2004).

444 30 Schouten, K. J. P., Qin, Z., Pérez Gallent, E. & Koper, M. T. Two pathways for the  
445 formation of ethylene in CO reduction on single-crystal copper electrodes. *J. Am. Chem.*  
446 *Soc.* **134**, 9864-9867 (2012).

447 31 Wang, Z., Cao, X.M., Zhu, J. & Hu, P. Activity and coke formation of nickel and nickel  
448 carbide in dry reforming: a deactivation scheme from density functional theory. *J. Catal.*  
449 **311**, 469-480 (2014).

450 32 Wang, Z., Wang, H.-F. & Hu, P. Possibility of designing catalysts beyond the traditional  
451 volcano curve: a theoretical framework for multi-phase surfaces. *Chem. Sci.* **6**, 5703-  
452 5711 (2015).

453 33 Liu, Q. *et al.* Approaching the capacity limit of lithium cobalt oxide in lithium ion  
454 batteries via lanthanum and aluminium doping. *Nat. Energy* **3**, 936-943 (2018).

455 34 Schreier, M., Yoon, Y., Jackson, M. N. & Surendranath, Y. Competition between H and  
456 CO for active sites governs copper-mediated electrosynthesis of hydrocarbon fuels.  
457 *Angew. Chem., Int. Ed.* **57**, 10221-10225 (2018).

458 35 Wang, L. *et al.* Electrochemical carbon monoxide reduction on polycrystalline copper:  
459 Effects of potential, pressure, and pH on selectivity toward multicarbon and oxygenated  
460 products. *ACS Catal.* **8**, 7445-7454 (2018).

461 36 Handoko, A. D., Wei, F., Yeo, B. S. & Seh, Z. W. Understanding heterogeneous  
462 electrocatalytic carbon dioxide reduction through operando techniques. *Nat. Catal.* **1**,  
463 922-934 (2018).

464 37 Razzaq, R., Li, C. & Zhang, S. Coke oven gas: availability, properties, purification, and  
465 utilization in China. *Fuel* **113**, 287-299 (2013).

466 38 Wang, S., Wang, G., Jiang, F., Luo, M. & Li, H. Chemical looping combustion of coke  
467 oven gas by using Fe<sub>2</sub>O<sub>3</sub>/CuO with MgAl<sub>2</sub>O<sub>4</sub> as oxygen carrier. *Energy Environ. Sci.* **3**,  
468 1353-1360 (2010).

469 39 Hoang, T. T. H., Ma, S. C., Gold, J. I., Kenis, P. J. A. & Gewirth, A. A. Nanoporous  
470 copper films by additive-controlled electrodeposition: CO<sub>2</sub> reduction catalysis. *ACS*  
471 *Catal.* **7**, 3313-3321 (2017).

472 40 Hoang, T. T. H. *et al.* Nanoporous copper silver alloys by additive-controlled  
473 electrodeposition for the selective electroreduction of CO<sub>2</sub> to ethylene and ethanol. *J. Am.*  
474 *Chem. Soc.* **140**, 5791-5797 (2018).

475 41 Ma, S. C. *et al.* One-step electrosynthesis of ethylene and ethanol from CO<sub>2</sub> in an alkaline  
476 electrolyzer. *J. Power Sources* **301**, 219-228 (2016).

477 42 Huang, Y., Handoko, A. D., Hirunsit, P. & Yeo, B. S. Electrochemical reduction of CO<sub>2</sub>  
478 using copper single-crystal surfaces: effects of CO\* coverage on the selective formation  
479 of ethylene. *ACS Catal.* **7**, 1749-1756 (2017).

480 43 Eren, B. *et al.* Activation of Cu(111) surface by decomposition into nanoclusters driven  
481 by CO adsorption. *Science* **351**, 475-478 (2016).

482 44 Eren, B. *et al.* One-dimensional nanoclustering of the Cu(100) surface under CO gas in  
483 the mbar pressure range. *Surf. Sci.* **651**, 210-214 (2016).

484 45 Li, J. *et al.* Copper adparticle enabled selective electrosynthesis of n-propanol. *Nat.*  
485 *Commun.* **9**, 4614 (2018).

486 46 Kresse, G. & Furthmuller, J. Efficient iterative schemes for ab initio total-energy  
487 calculations using a plane-wave basis set. *Phys. Rev. B* **54**, 11169-11186 (1996).

488 47 Kresse, G. & Furthmuller, J. Efficiency of ab-initio total energy calculations for metals  
489 and semiconductors using a plane-wave basis set. *Comput. Mater. Sci.* **6**, 15-50 (1996).

490 48 Kresse, G. & Hafner, J. Ab-initio molecular-dynamics simulation of the liquid-metal  
491 amorphous-semiconductor transition in germanium. *Phys. Rev. B* **49**, 14251-14269  
492 (1994).

493 49 Kresse, G. & Hafner, J. Ab initio molecular dynamics for liquid metals. *Phys. Rev. B* **47**,  
494 558-561 (1993).

495 50 Perdew, J. P., Burke, K. & Ernzerhof, M. Generalized gradient approximation made  
496 simple. *Phys. Rev. Lett.* **77**, 3865-3868 (1996).

497 51 Kresse, G. & Joubert, D. From ultrasoft pseudopotentials to the projector augmented-  
498 wave method. *Phys. Rev. B* **59**, 1758-1775 (1999).

499 52 Blochl, P. E. Projector augmented-wave method. *Phys. Rev. B* **50**, 17953-17979 (1994).

500 53 Grimme, S., Antony, J., Ehrlich, S. & Krieg, H. A consistent and accurate ab initio  
501 parametrization of density functional dispersion correction (DFT-D) for the 94 elements  
502 H-Pu. *J. Chem. Phys.* **132**, 154104 (2010).

503 54 Alavi, A., Hu, P., Deutsch, T., Silvestrelli, P. L. & Hutter, J. CO oxidation on Pt (111):  
504 An ab initio density functional theory study. *Phys. Rev. Lett.* **80**, 3650 (1998).  
505 55 Michaelides, A. *et al.* Identification of general linear relationships between activation  
506 energies and enthalpy changes for dissociation reactions at surfaces. *J. Am. Chem. Soc.*  
507 **125**, 3704-3705 (2003).  
508 56 Liu, Z. P. & Hu, P. General rules for predicting where a catalytic reaction should occur  
509 on metal surfaces: a density functional theory study of C–H and C–O bond  
510 breaking/making on flat, stepped, and kinked metal surfaces. *J. Am. Chem. Soc.* **125**,  
511 1958-1967 (2003).  
512 57 Shang, Y., Zhang, D. F. & Guo, L. CuCl-intermediated construction of short-range-  
513 ordered Cu<sub>2</sub>O mesoporous spheres with excellent adsorption performance. *J. Mater.*  
514 *Chem.* **22**, 856-861 (2012).  
515 58 Jhong, H. R. M., Brushett, F. R. & Kenis, P. J. The effects of catalyst layer deposition  
516 methodology on electrode performance. *Adv. Energy Mater.* **3**, 589-599 (2013).

## 517 **Acknowledgements**

518 This work was supported financially by the Ontario Research Fund Research-Excellence  
519 Program, the Natural Sciences and Engineering Research Council (NSERC) of Canada, the  
520 CIFAR Bio-Inspired Solar Energy program, and the University of Toronto Connaught grant.  
521 This research used synchrotron resources of the Advanced Photon Source (APS), an Office of  
522 Science User Facility operated for the U.S. Department of Energy (DOE) Office of Science by  
523 Argonne National Laboratory, and was supported by the U.S. DOE under Contract No. DE-  
524 AC02-06CH11357, and the Canadian Light Source and its funding partners. This research also  
525 used infrastructure provided by the Canada Foundation for Innovation and the Ontario Research  
526 Fund. The authors thank Dr. T.P. Wu, Dr. Y.Z. Finfrock and Dr. L. Ma for technical support at  
527 9BM beamline of APS. D.S. acknowledges the NSERC E.W.R Steacie Memorial Fellowship.  
528 J.L. acknowledges the Banting Postdoctoral Fellowships program. C.G acknowledges the  
529 NSERC Postdoctoral Fellowships program. All DFT computations were performed on the IBM  
530 BlueGene/Q supercomputer with support from the Southern Ontario Smart Computing  
531 Innovation Platform (SOSCIP). SOSCIP is funded by the Federal Economic Development  
532 Agency of Southern Ontario, the Province of Ontario, IBM Canada Ltd., Ontario Centres of  
533 Excellence, Mitacs and 15 Ontario academic member institutions.

## 534 **Author contributions**

535 E.H.S and D.S. supervised the project. J.L. designed and carried out all the experiments. Z.Y.W.  
536 performed the DFT simulation. C.M. simulated the diffusion-reaction. J.Y.H. conducted the  
537 SEM characterization. F.W.L., L.W., and Y.R. assisted the operando XRD measurements and

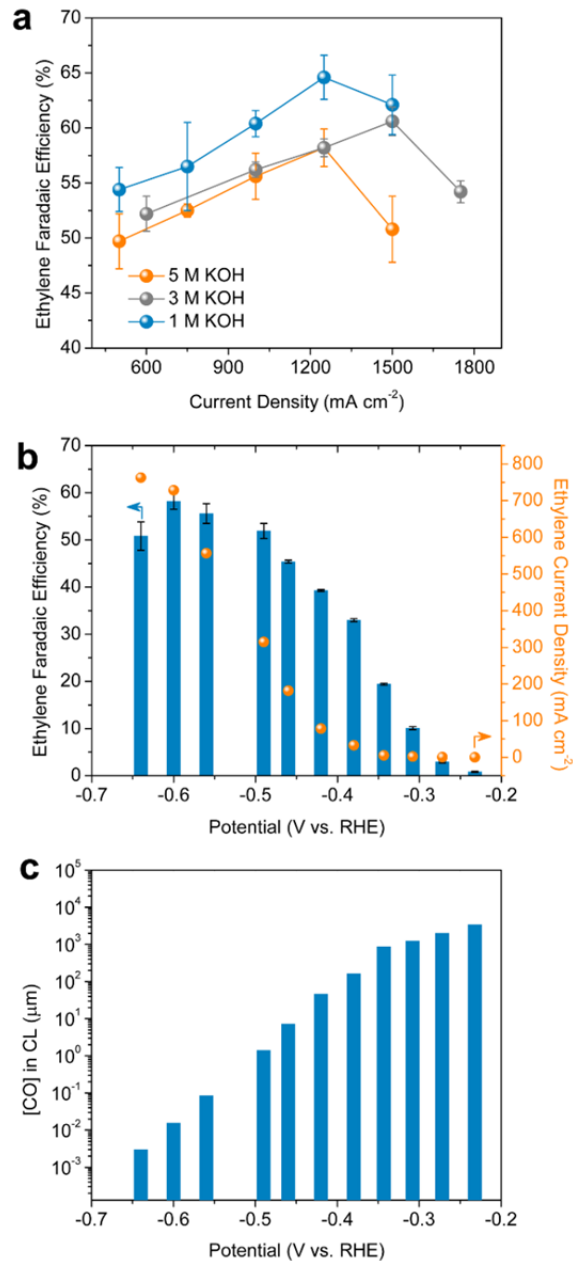
538 data analysis. Y.X., Y.H.W., C.G., C.T.D. and T.T.Z. contributed in data analysis and manuscript  
539 polishing. All authors discussed the results and assisted during manuscript preparation.

540 **Competing interests**

541 The authors declare no competing interests.

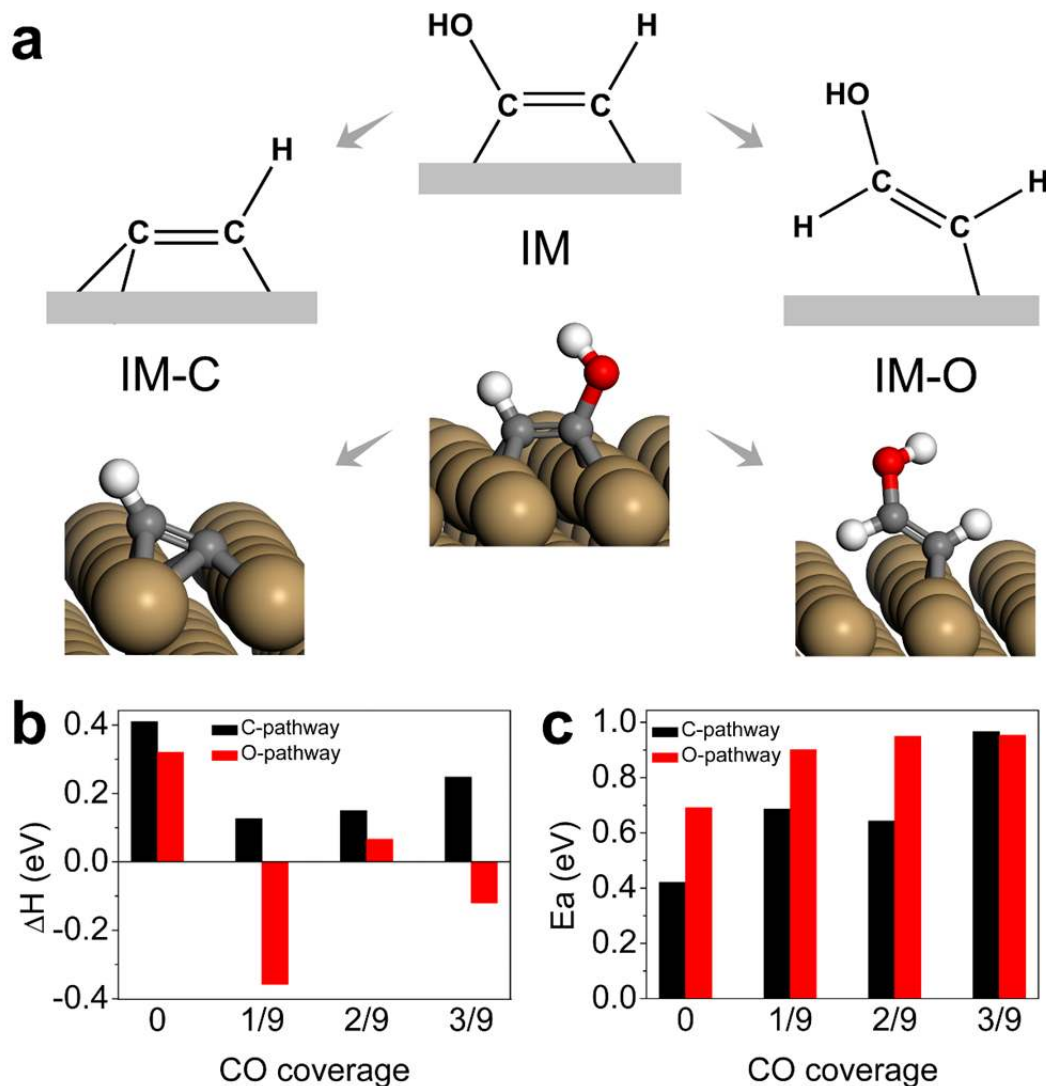
542





543  
 544 **Fig. 1. Influence of KOH concentration on CO reduction.** **a**, A comparison of ethylene  
 545 Faradaic efficiency at various KOH concentrations as a function of applied current density. **b**,  
 546 Ethylene Faradaic efficiency and partial current density from CO reduction in 5 M KOH as a  
 547 function of applied potential. **c**, Simulated local CO concentration [CO] in the catalyst layer (CL)  
 548 as a function of applied potential in 5 M KOH. Error bars are means  $\pm$  SD (n = 3 replicates).

549



550

551 **Fig. 2. DFT calculation results on effects of \*CO coverage. a,** Schematic plot of reaction

552 mechanisms of removing the last oxygen-containing group in \*CHCOH (IM) to \*CCH (IM-C),

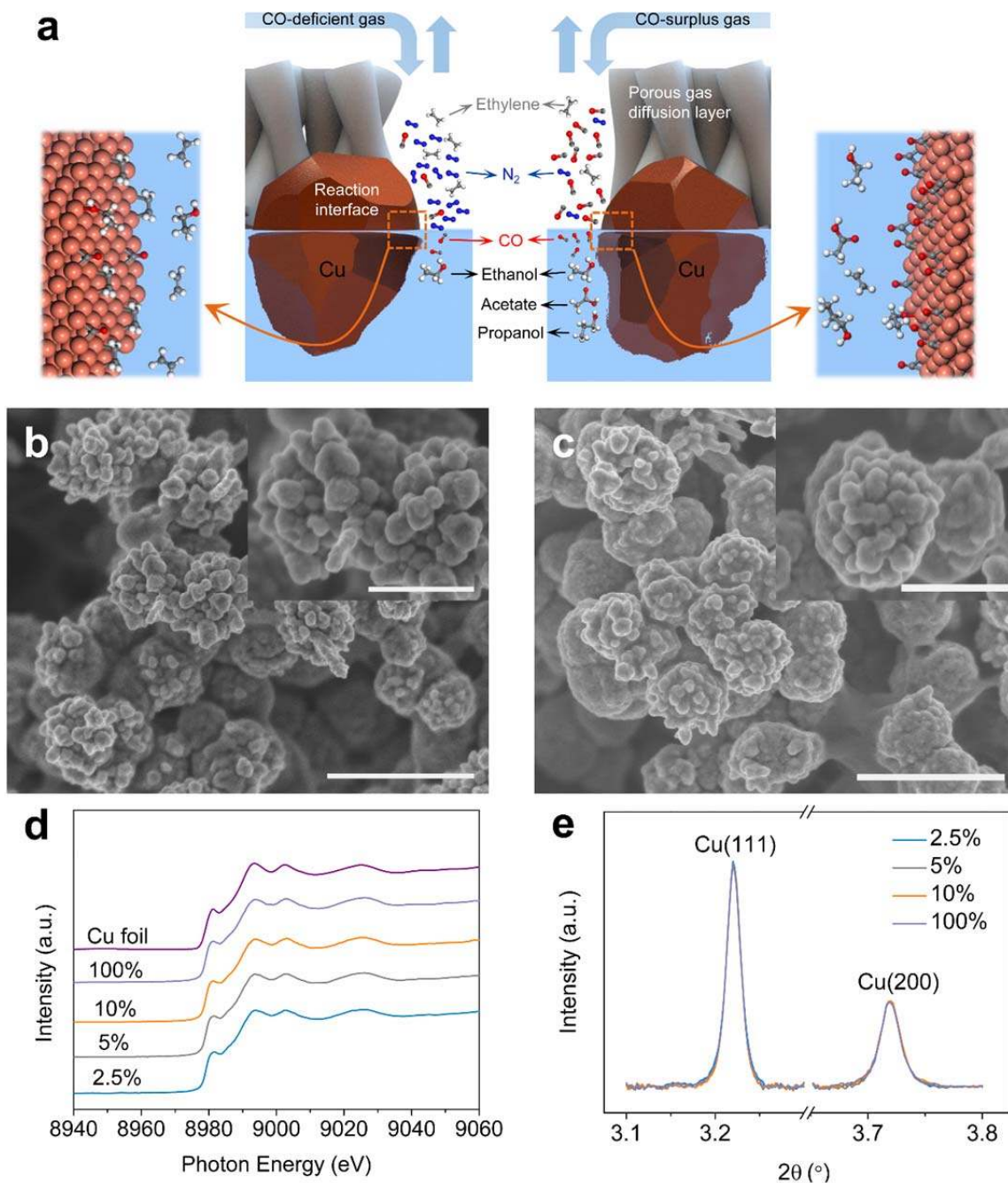
553 and alternative pathway to \*CHCHOH (IM-O), as well as the geometries of IM, IM-C and IM-O

554 on Cu(100) surfaces. Yellow, grey, red, and white balls stand for Cu, C, O, and H, respectively.

555 **b,** The enthalpy change for the C- and O-pathways at different levels of CO coverage. **c,** The

556 relation between coverage and activation energy of these two pathways.

557



558

559 **Fig. 3. Characterization of the Cu electrocatalysts.** a, Schematic illustration of porous gas

560 diffusion electrodes with CO reduction at the catalyst-electrolyte interface showing conditions of

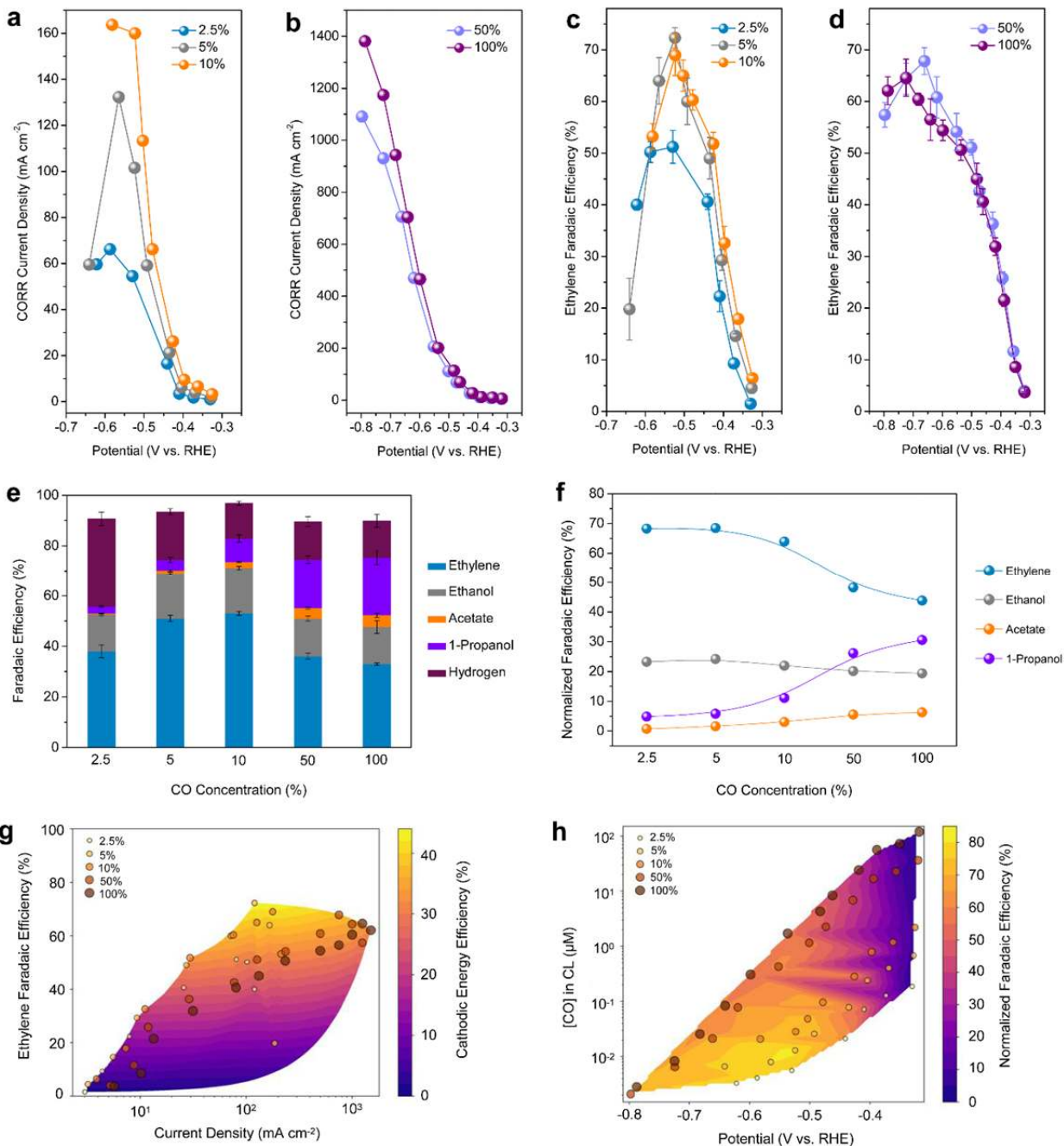
561 CO-deficiency and CO-surplus influencing production. b, c, SEM images of derived Cu catalysts

562 at CO concentrations of 100% (b) and 2.5% (c); The scale bars are both 500 nm. Insets are

563 respective high-resolution SEM results with scale bars of 200 nm. d, e, Operando Cu K-edge

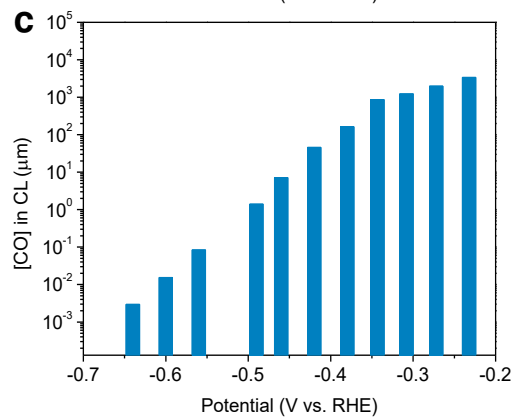
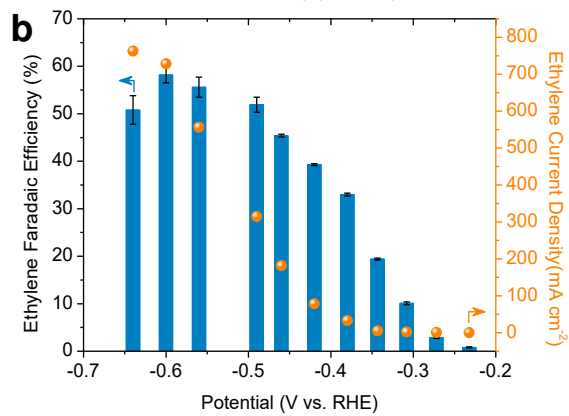
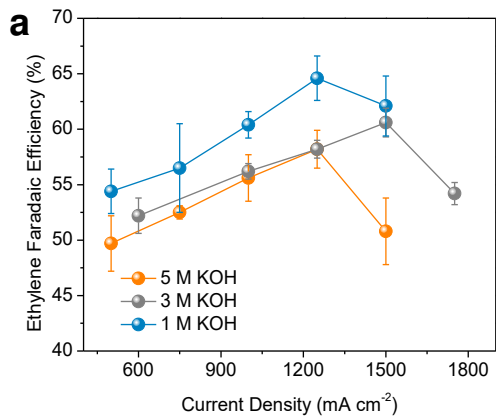
564 XAS (**d**) and high-resolution operando XRD (**e**,  $\lambda=0.4593 \text{ \AA}$ ) results of derived Cu catalysts at  
565  $100 \text{ mA cm}^{-2}$  in 1 M KOH at various CO concentrations. Ex-situ Cu K-edge XAS of Cu foil is  
566 included in (**d**) as a reference.

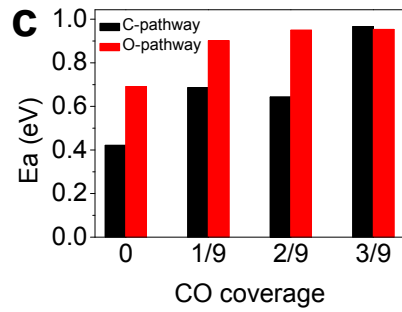
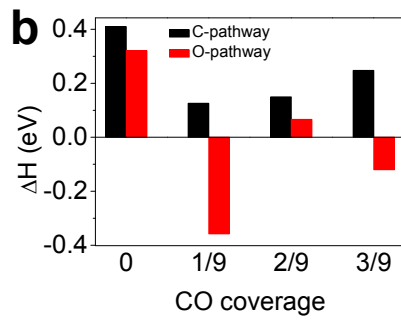
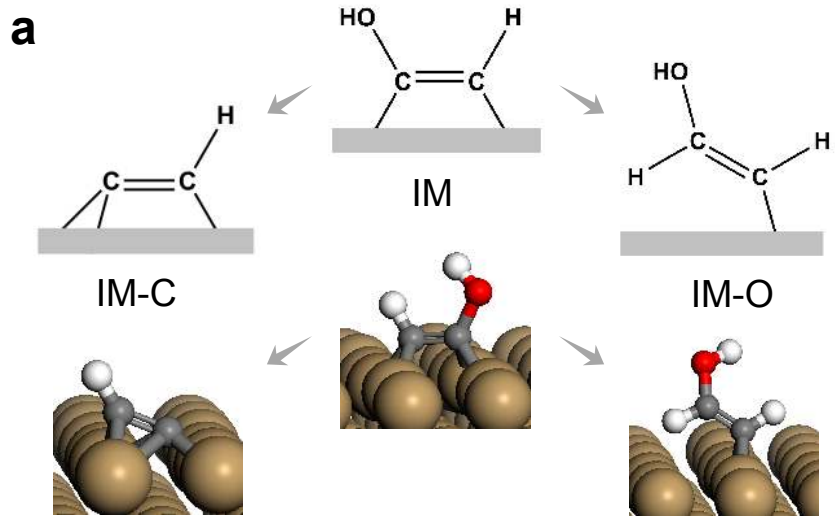
567



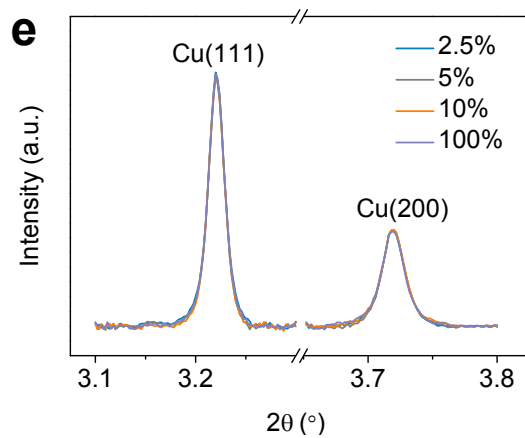
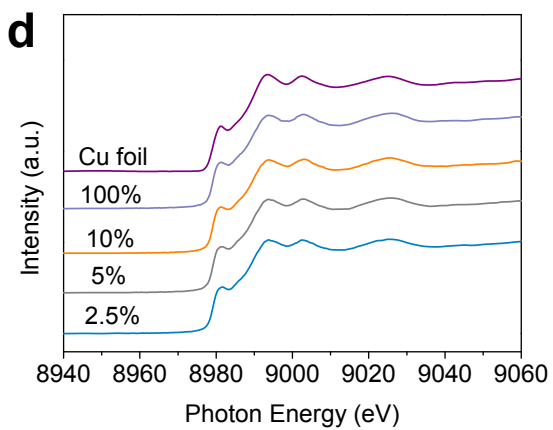
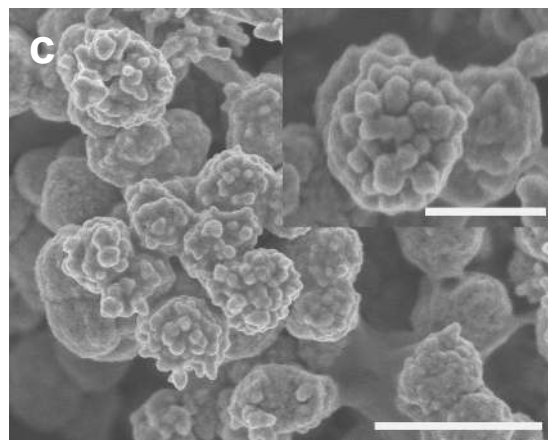
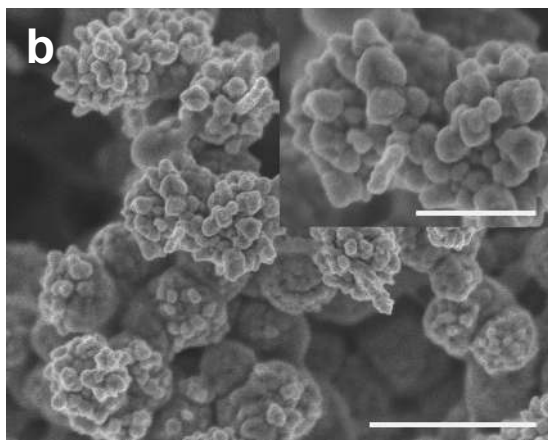
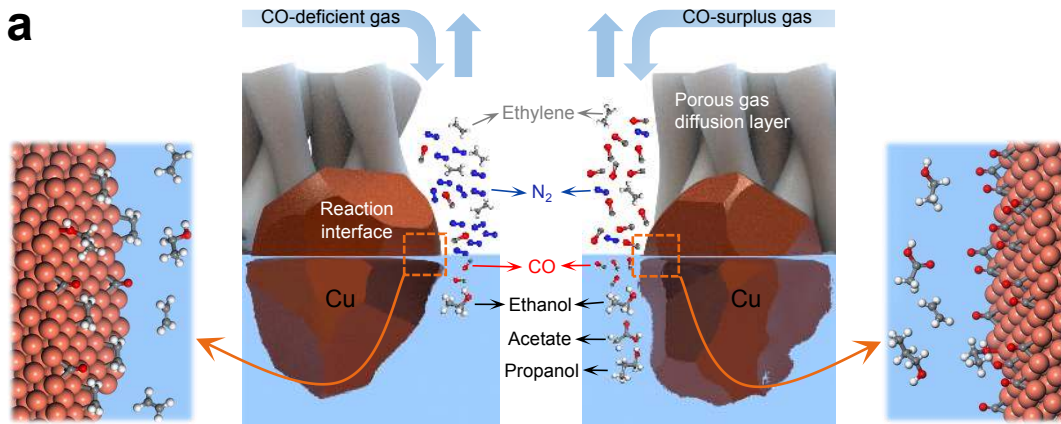
568  
 569 **Fig. 4. CORR performance as a function of CO coverage. a-d**, CORR partial current densities  
 570 **(a, b)** and ethylene Faradaic efficiency **(c, d)** at various CO concentrations as a function of  
 571 applied potential in 1 M KOH. **e, f**, Faradaic efficiencies **(e)** and normalized Faradaic efficiencies  
 572 **(f)** of CORR products at different CO concentrations at an applied potential of -0.44 V vs. RHE  
 573 in 1 M KOH. **g**, Mapping of the cathodic energy efficiency and ethylene Faradaic efficiency as a

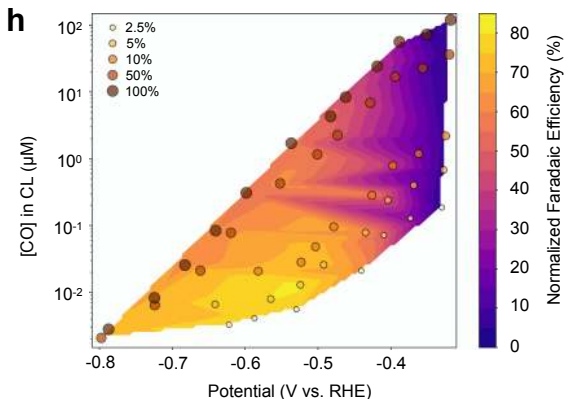
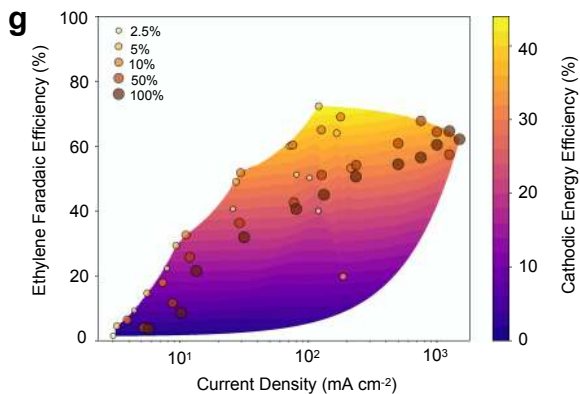
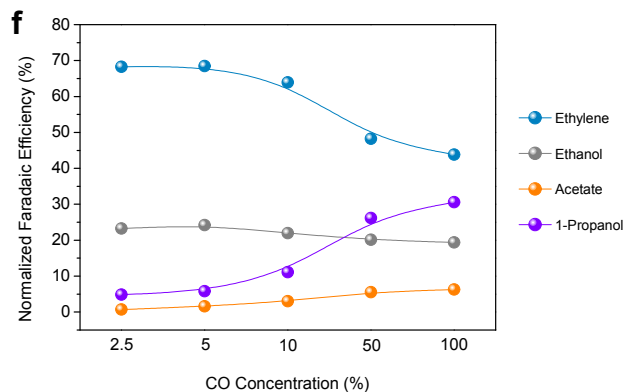
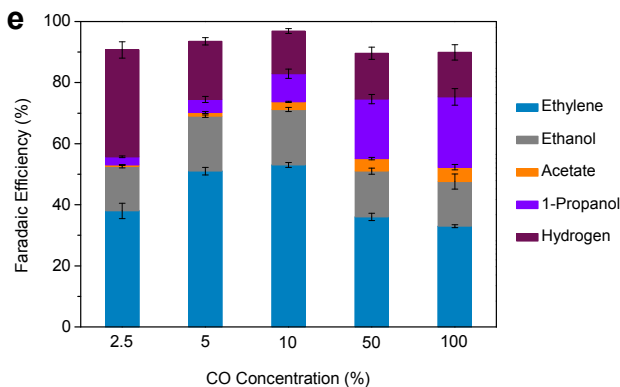
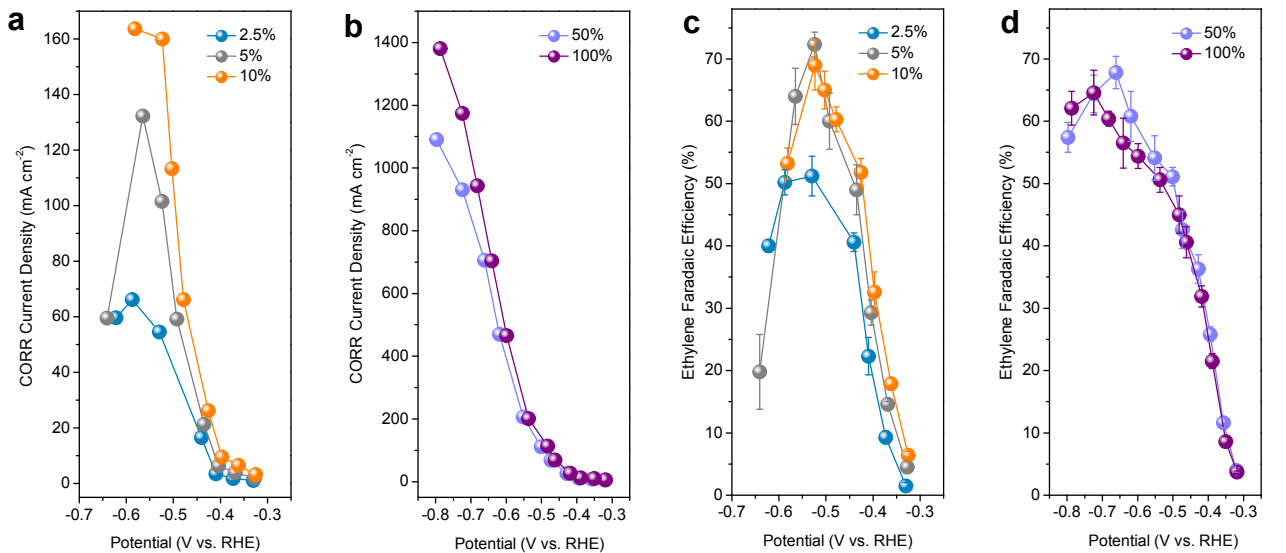
574 function of current density. **h**, Mapping of the normalized ethylene Faradaic efficiency and  
575 simulated local CO concentration [CO] in the catalyst layer (CL) as a function of applied  
576 potential. Error bars are means  $\pm$  SD (n = 3 replicates). The heatmap in **g** was generated via  
577 linear interpolation using the `griddata` function of `scipy` (in *Python 3.6*) to interpolate between  
578 points and illustrate the broader relationships between current density, ethylene Faradaic  
579 efficiency and cathodic energy efficiency. The heatmap values were interpolated from  
580 experimental values. Similarly, the heatmap in **h** was generated via linear interpolation to  
581 highlight the effect of simulated local CO concentration and applied potential on the normalized  
582 ethylene Faradaic efficiency.











**Cu** electrocatalysts

